A R C H I V E O F M E C H A N I C A L E N G I N E E R I N G

Volume 67 2020 Number 1

DOI: 10.24425/ame.2020.131681

Key words: marine structures, blast waves, failure models, FSI, UNDEX

Arman Jafari Valdani[1], Armen Adamian[1]

Finite element-finite volume simulation of underwater explosion and its impact on a reinforced steel plate

Marine structures are one of the most important industrial and military equipment in each country that should be protected against external forces. The main aim of this paper is a detailed investigation of the underwater explosion (UNDEX) and its effects on marine structures. For this purpose, the UNDEX structure was studied qualitatively and quantitatively using numerical methods. Then, the effects of blast waves on a marine structure reinforced by perpendicular blades were investigated. Finite element and finite volume schemes were used for discretization of the governing equations in the solid and fluid media, respectively. Also, for fluid-structure interaction (FSI), results of fluid and solid media were mapped to each other using the two-way FSI coupling methods. A comparison of numerical results with the empirical formula revealed that the trend of pressure-time curves was reasonable, approving the validity of the numerical method. Moreover, the numerical results indicated that detonation of 1 kg trinitrotoluene (TNT) creates a pressure wave with maximum amplitude of 24 MPa at a distance of 2 m. Also, it was found that the reinforcement blades can be used to improve the resistance of structures against explosive charges, which also results in the reduction of structures deformation.

1. Introduction

Considering the importance of marine structures such as bridges, dams, ships and submarines, various analytical [1–4], experimental [5–7], and numerical [8–10] studies have been conducted in the field of UNDEX. Among these research tools, numerical methods are less costly, produce extensive results, and are able to solve complicated problems [11, 12]. These features make the numerical method as a robust tool for researchers in different fields.

✉ Armen Adamian, e-mail: arm.adamian@iauctb.ac.ir

[1]Department of Mechanical Engineering, Central Tehran Branch, Islamic Azad University, Tehran, Iran.

Generally, four different numerical methods, including Finite Element Method (FEM), Finite Volume Method (FVM), Boundary Element Method (BEM), and Smooth Particle Hydrodynamics (SPH) were used to solve UNDEX problems [13]. The FEM is the most common method to simulate the behavior of solid materials and is capable of considering nonlinear impacts. In this method, the boundary conditions are applied in surfaces or nodes [14]. Gupta et al. [15] showed the precision of FEM in reproducing the dynamic response of steel panels to UNDEX. Also, FVM is conventionally used to simulate the behavior of fluid materials. In this method, both structured and unstructured elements could be utilized to generate a grid structure. For each control volume, the conservative laws are discretized, and partial differential equations are converted to the linear system of equations. Ma et al. [16] proved the accuracy of FVM by solving one, two, and three-dimensional UNDEX problems. Wang et al. [17] used the FVM to develop a simple model for determining the appropriate grid size in near-field UNDEX simulations. Unlike FEM and FVM, the grid generation in BEM is more straightforward, which could give highly accurate results in complex geometries. Li et al. [18] showed that BEM gives precise results in the problems that involve stress concentrations. In this method, the matrix of the system of equations is fully populated and asymmetric. Also, its conditioning number is not high enough. Therefore, obtaining numerical results may imply some mathematical difficulties [19]. Gong and Khoo [20] used the coupled BEM-FEM to simulate the interaction of UNDEX and composite structures. Moreover, the SPH method has some advantages compared to the above-mentioned methods due to its mesh-free solving scheme. Because of this unique feature, even problems with very complex boundary dynamics and large deformations could be numerically solved. On the other hand, the computational cost of this method is significantly increased by increasing the number of particles [21]. Using SPH method, various UNDEX problems have been modeled by Ming et al. [22]. They validated the accuracy of the SPH method by comparing the results with the experimental data.

Various physical processes such as a near-field explosion, FSI, and large deformations should be considered to study the effects of UNDEX on structures. The Lagrangian and Eulerian methods are two primary computational approaches to deal with these processes properly. In the Lagrangian approach, structural mesh moves and deforms with the physical material allowing accurate prediction of structural behavior [20, 23, 24]. However, in large deformations, the grids are severely distorted or tangled, which decreases the accuracy of results. In the Eulerian approach, the grids are fixed in space, and the material flows through them. Therefore, there is no mesh distortion, even in the case of large deformations. The disadvantage of the Eulerian approach is the accumulation of advection and interface tracking errors [25].

Studies on UNDEX have been performed to improve the safety of two main marine structures: 1) concrete structures (dams) and 2) steel structures (ships and submarines). In the field of concrete structures, Linsbauer [26] used the coupled

model of water and dam reservoir and studied the dynamic characteristic, stability, and destruction mechanism of concrete gravity dams under the impact of blast loading. The simulations were carried out using SOL03 software, which is based on FEM. Zhang et al. [27] investigated the material properties for accurate prediction of the UNDEX effects on concrete dams. To simulate the response of concrete dams at heights of 30 to 142 m against blast waves, they determined appropriate grid generation scheme in LS-DYNA software (based on the FEM), as well as proper boundary conditions. The imposed damage caused by the explosion near the water dams was estimated, and the failure rates, as well as critical states, were plotted for different explosion scenarios. Furthermore, Wang and Zhang [25] predicted the response of a typical concrete gravity dam subjected to UNDEX using numerical simulation. In their study, TNT, air, and water were modeled using the Eulerian approach, while the Lagrangian approach was used to model the concrete and rock. The results were used to derive critical curves related to different damage levels.

In the field of the effects of UNDEX on steel structures, Rajendran [28] studied the elastic and plastic response of circular and rectangular plates using LS-DYNA. Gupta et al. [15] simulated the failure modes of a plate subjected to UNDEX using FEM by considering the effects of isotropic hardening, strain rate, and fracture criterion. Zhang et al. [29] investigated damages to the ships caused by explosive charges using numerical methods. The numerical model was constructed using ABAQUS software based on FEM. In this study, the numerical results were validated against experimental data, and then, the responses of a ship against different explosive scenarios were simulated. The results indicated that the position of the explosive charge has a direct impact on the ship's failure rate. Fathallah et al. [30] also studied the effect of UNDEX on steel structures. They used ABAQUS software to study the effect of explosive charges on various metal structures. Also, they adopted non-reflective boundary conditions in their analysis to prevent from shockwave refraction or reflection, which could result in superposition or cancellation of shock waves by the incident wave. The results of this study can be used to optimize floating structures in water such as ships and submarines. Qiankun and Gangyi [31] employed ABAQUS software to predict the shock response of a ship to non-contact UNDEX. The results emphasized that the grid size has a great impact on the accuracy of the numerical results. Wang et al. [32] studied the characteristics of the generated blast waves from near-surface explosions using numerical methods. Using the Eulerian/Lagrangian viewpoint along with the two-way FSI coupling method, they simulated the UNDEX and investigated its effects on structures. In the simulations, the governing equations in the Eulerian and Lagrangian domains were solved using FVM and FEM, respectively. The results revealed that the free and structure surface boundaries have a significant influence on the results indicating that adaptation of the appropriate boundary conditions is a necessity in UNDEX simulations. Liu et al. [7] studied FSI problems with considering strain rates experimentally and numerically. They utilized ABAQUS software and the

numerical method was based on FEM. Moreover, the steel plate was modeled using the Lagrangian approach. The results indicated that it is necessary to consider the effect of the strain rate in the strength equation to obtain valid and accurate results. LeBlanc and Shukla [33] used LS-DYNA software to simulate the effects of polyurea coatings on the UNDEX response of composite plates. The effects of fluid on the structure were considered utilizing a mesh that was equivalence at the boundary between the fluid domain and composite plate. Comparison of numerical and experimental results showed that FEM and material models are capable of simulating the dynamic loading of the plate and the corresponding transient responses.

In the present study, to investigate the UNDEX in detail, the structure of the detonation wave was numerically simulated using coupled FEM/FVM. First, the amplitude and velocity of blast waves were analyzed qualitatively and quantitatively. Afterward, by 3D simulation of steel plate reinforced by perpendicular blades, the efficiency of these stiffeners to improve the strength of marine structures against explosive loads was explored.

2. Problem description

2.1. Structure of TNT explosion and empirical formulas

The physical phenomenon associated with UNDEX begins with the conversion of the explosive charge into high-temperature and high-pressure gas products. This process generates a shock wave with supersonic speed. The shock wave is instantly followed by a reaction zone in which the chemical reaction occurs. The chemical energy released by explosives such as TNT supports the shock wave and increases the pressure. In the unconfined UNDEX, the generated pressure wave is transmitted spherically through the surrounding water in all directions. The trapped gases in the explosion form expanding bubbles, which push the surrounding water outward. At later times, due to the outward movement of water, the gas pressure falls below the ambient pressure. This negative pressure gradient decelerates the surrounding water and changes the direction of particles. Interaction of bubble movement and water inertia creates an oscillating system with repeated cycles of expansions and contractions of the gas bubble. This process could create a secondary pressure wave that is considerably weaker than the primary shock wave [34, 35]. Zamyshlyayev and Yakovlev [1] developed a precise and widespread formula to predict the structure of UNDEX pressure waves. In fact, the pressure distribution was predicted in different stages using the following equations [1, 11]:

$$P(t) = P_m \exp(-t/\theta), \qquad \text{for } t < \theta, \tag{1}$$

$$P(t) = 0.368 P_m (\theta/t) \left[1 - (t/t_P)^{3/2}\right] \qquad \text{for } \theta \leqslant t \leqslant t_1, \tag{2}$$

where P in Equations (1) and (2) is the pressure of a specific point at exponential decay and reciprocal decay stages, respectively. In these equations, P_m and θ are the peak pressure of the shock wave and its related occurrence time which could be calculated using the following formulas [1, 11]:

$$P_m = \begin{cases} 4.41e7 \left(\dfrac{W^{1/3}}{R}\right)^{3/2} & \text{for } 6 < \bar{r} < 12, \\ 5.24e7 \left(\dfrac{W^{1/3}}{R}\right)^{3/2} & \text{for } 12 \leqslant \bar{r} < 240, \end{cases} \tag{3}$$

$$\theta = \begin{cases} 0.45 R_0 \bar{r}^{0.45} e - 3 & \text{for } \bar{r} < 30, \\ 3.5 \dfrac{R_0}{C} \sqrt{\log \bar{r} - 0.9} & \text{for } \bar{r} \geqslant 30, \end{cases} \tag{4}$$

where W is mass of TNT, R is the distance between detonation point and measuring location, R_0 is the initial radius of spherical explosive, and $\bar{r} = R/R_0$.

2.2. Numerical domain

To investigate the UNDEX, a geometry same as those employed in the analytical study of Zamyshlyayev and Yakovlev [1], as well as the numerical study of Xin et al. [11] were considered. Zamyshlyayev and Yakovlev [1] solved the governing equations on 1D UNDEX using simplifying assumptions and presented a mathematical-empirical model for pressure calculation. Accordingly, in the present study, the explosion of 1 kg of TNT in water media is simulated, and the results were recorded at different times. A general schematic of the problem is shown in Fig. 1. In this figure, the monitoring gauge points at a distance of 2, 4, 6,

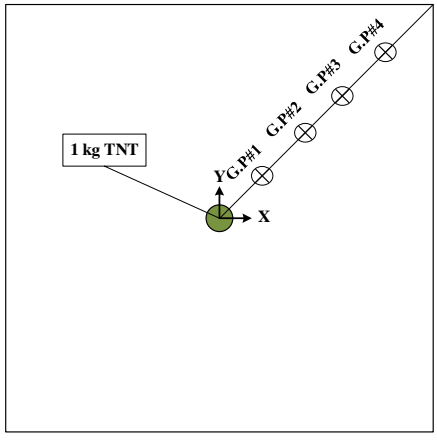

Fig. 1. Schematics of the problem-monitoring gauge points are shown with ⊗ symbol

and 8 m from the detonation point are shown with ⊗ symbol and the initial position of explosive charge is indicated with green color. In this problem, geometry and boundary conditions have spherical symmetry. In other words, in an unconfined UNDEX, the gradients of parameters in θ and φ coordinates are zero, and changes only occur in r direction. Therefore, to reduce the computational costs, the simulations were performed based on a spherical symmetry assumption. In this regard, a wedge from a sphere that has symmetry conditions on side edges limited by a non-reflective outflow condition at $r = R_{\max}$ was considered, as shown in Fig. 2. The non-reflective boundary condition was used to model the infinite media (such as unconfined UNDEX), which allows pressure waves to pass through boundaries without affecting the numerical domain [30]. In this figure, the green zone is the initial location of the TNT explosive, and the blue zone is the initial location of the water media extended for 10 m. This value was chosen in such a way that numerical results were not affected by boundary conditions. Also, the pressure monitoring points are depicted by numbers 1 to 4.

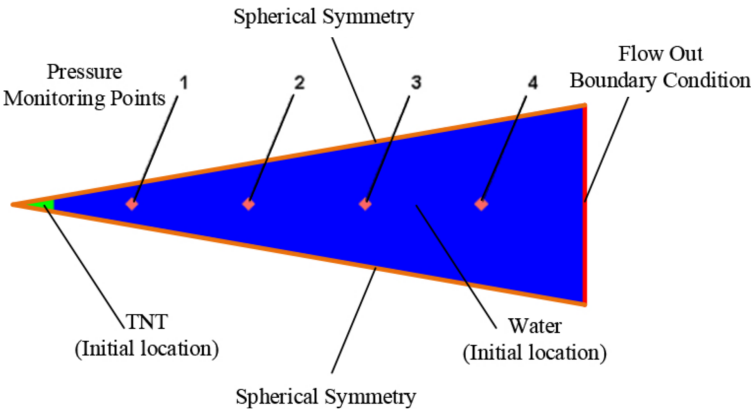

Fig. 2. Details of the 2D numerical model – initial location of materials and boundary conditions

In the second part of the paper, the effects of blast wave generated due to the explosion of 500 g of TNT at a distance of 260 mm from the barrier are investigated. A general schematic of the problem is shown in Fig. 3. In this figure, the hatched area represents the outer surface of the barrier, which is a square steel plate with 3 m sides and has a thickness of 20 mm. Nine stiffener blades are used to reinforce this plate. Moreover, the adopted boundary conditions are determined in this figure. In Fig. 4, the plate and its stiffeners are represented in isometric view. It is clear that the stiffener blades are perpendicular to each other.

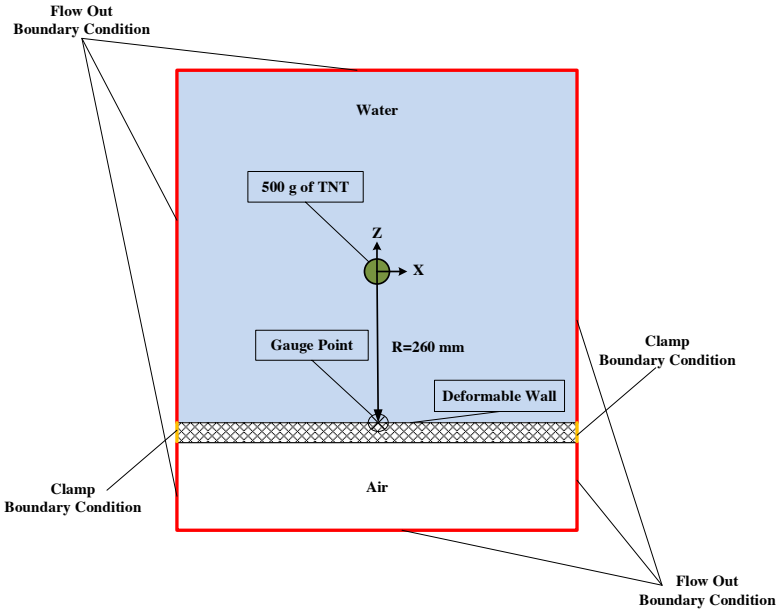

Fig. 3. Schematics of the modeled as well as adopted boundary conditions

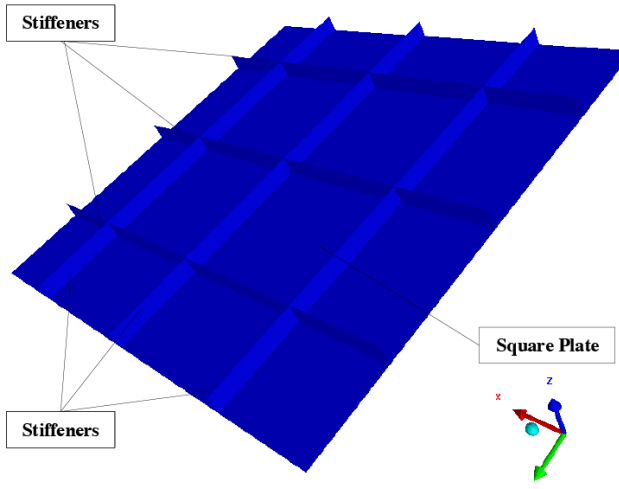

Fig. 4. Steel square plate with nine stiffener blades

2.3. Boundary and initial conditions

In the numerical simulations, the physics of the problem should be considered to assign the boundary conditions of the numerical domain properly. Hence, in an unconfined UNDEX, the transmit boundary condition (non-reflective flow out) is considered in the boundaries next to water media to prevent the reflection of

pressure waves from boundaries. This boundary condition enables the material pressure flowing out without being reflected into the domain and is described according to the Equation (5) [36]:

$$P = \begin{cases} P_{\text{ref}} + (U_n - U_{\text{ref}})\, I & \text{for } U_n > 0 \\ P_{\text{ref}} & \text{for } U_n \leqslant 0 \end{cases} \tag{5}$$

where U_n and P are normal velocity and pressure at the boundary; U_{ref} and P_{ref} are the reference velocity and pressure, respectively. Additionally, I is the material impedance, which is defined as $I = \rho \times \textit{sound speed}$. Details of other boundary conditions and implemented areas are described in Table 1. The applied boundary conditions are also clearly shown in Fig. 2 and Fig. 3.

Table 1.

Used boundary conditions along with their characteristics

Type	Applied parts	Characteristics
Flow out	Eulerian	Materials are allowed to enter or leave the computational domain. Inlet flow has ambient conditions.
Clamp	Lagrangian	This condition is equivalent to the fixed support, and all velocity components are zero.
Symmetry	Eulerian and Lagrangian	Changes in the normal direction to the desired plane are zero.

Another issue in the numerical methods is setting proper initial conditions in the computational domain. The initial conditions include the state (velocity), the internal energy (temperature), and the pressure of the materials at $t = 0$. The initial conditions are determined according to the conditions of the problem in which the velocity component is equal to zero (quiescent condition), and the temperature is equal to 298 K (ambient condition).

3. Description of numerical method

3.1. Fluid-structure interaction description

Due to the presence of solid and fluid media as well as their influence on each other, FSI should be considered in the numerical method. This method is based on solving the governing equations of the fluid and solid media in which the interaction between the fluid and the structure is considered in terms of the pressure, stress, and velocity distribution in the overall numerical domain [37]. The numerical method in the fluid-structure coupling problems is rewritten to three smaller sub-solvers [23, 38]: sub-solver of the fluid medium, sub-solver of the solid medium, and coupling sub-solver (Fig. 5). In the present numerical model, the two-way (fully-coupled) FSI algorithm is used in the third sub-solver. In this method, the effects

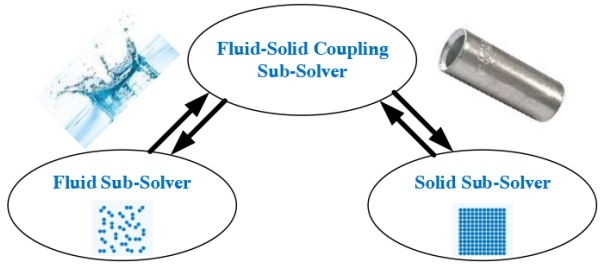

Fig. 5. Connections between fluid, solid and coupling sub-solver on an FSI simulation

of fluid and solid media on each other are considered through numerical iteration on each time step. When there are no changes in the fluid and structure states, the iteration is ended, and next time step starts. These concepts are summarized in an algorithm as shown in Fig. 6. Also, the detailed description of the FSI condition in the numerical simulation is presented in Table 2. In this table, interaction domains and coupling methods in each environment with mutual boundaries are presented. As shown in Fig. 6, in the fully-coupled algorithm the iteration continues while reaching the convergence criteria. While this concept increases the computational cost, the accuracy of the results is also improved.

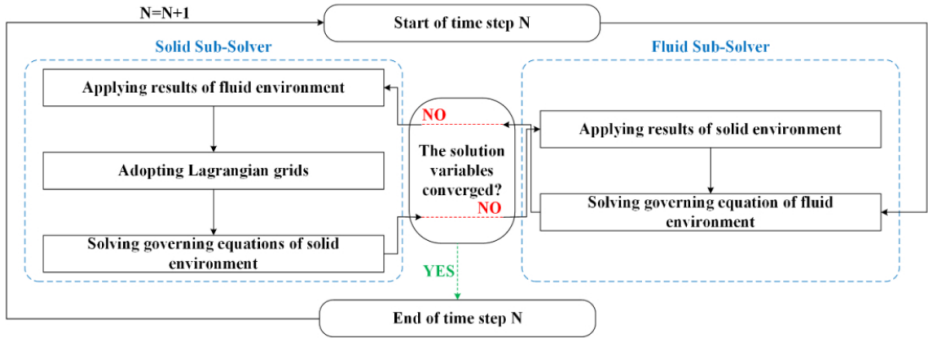

Fig. 6. Two-way FSI algorithm in the numerical simulations

Table 2.

Details of the applied FSI conditions in the simulations

Interaction boundaries	Interaction domains	Coupling method
Water/Plate	Eulerian/Lagrangian	Two-way/fully-coupled
Air/Plate	Eulerian/Lagrangian	Two-way/fully-coupled
Plate/Plate	Lagrangian/Lagrangian	Self-interaction/fully-coupled

It should be noted that the water and air domains are modeled by the Eulerian approach, while the Lagrangian approach is used to model the plate. As mentioned before, in the Lagrangian approach, the material remains in the element and does

not flow inward or outward. As a result, the numerical elements deform according to the material flow, as shown in Fig. 7. The coordinates, velocities, forces, and masses in each element are associated with the corner nodes, while stresses, strains, pressures, energies, and densities are centered within the cells [39, 40]. In contrast, the Eulerian approach involves material flow through stationary elements, as shown in Fig. 7. As the material moves from one element to the other, the time series of material properties, material interfaces, and free surfaces cannot be tracked as accurately as in a Lagrangian approach. The material flow also necessitates the use of advection algorithms in the Eulerian solvers making them more complex and more computationally expensive than Lagrangian solvers. In the Eulerian solver, all variables are cell-centered in a mesh, which facilitates coupling with other solvers required to address FSI problems [41].

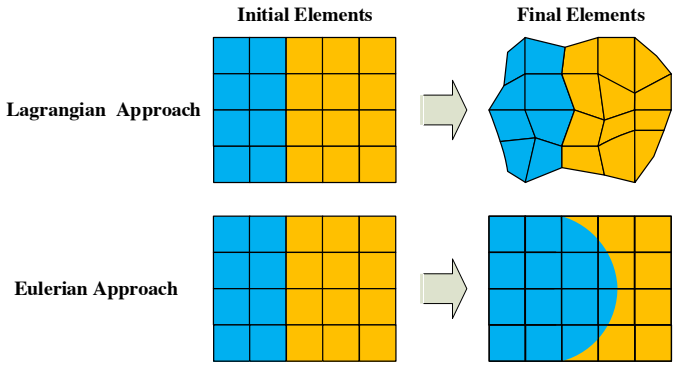

Fig. 7. Connections between fluid, solid and coupling sub-solver on an FSI simulation

3.2. Pressure wave reflection

In the numerical simulations, two types of conditions are considered for the blast wave when it reaches a boundary or a solid surface. As discussed before, all external boundaries are considered as a non-reflective transmit boundary. Hence, when a blast wave reaches to the boundaries, it flows out of the numerical domain without any reflection. In fact, in the real problems, the water media has infinite dimension; therefore, the limited domain in the numerical simulation should not reflect the pressure waves at the boundaries. In the second condition, when a blast wave reaches a solid surface, it is reflected, resulting in FSI and a transfer of energy from the wave to the surface. To accurately model this behavior, the two-way coupling method is considered in FSI coupling sub-solvers. In this method, mass, energy, and momentum are transferred in the form of boundary conditions from the Eulerian grid to the Lagrangian grid and vice-versa. In the numerical simulation, the Eulerian elements intersected by the Lagrangian interface act as a pressure boundary for the Lagrangian elements while the Lagrangian elements act as a geometric boundary on the material flow in the Eulerian elements [41].

3.3. Governing equations

Three main governing equations in the fluid media are the conservation laws of mass, momentum, and energy, which are presented as following [42]:

$$\frac{\partial \rho}{\partial t} + \nabla \cdot (\rho U) = 0, \tag{6}$$

$$\frac{\partial \rho U}{\partial t} + \nabla \cdot (\rho U * U) = \nabla \cdot \left(-\rho\delta + \mu\left(\nabla U + (\nabla U)^T\right)\right) + S_M, \tag{7}$$

$$\frac{\partial \rho h_{\text{tot}}}{\partial t} - \frac{\partial P}{\partial t} + \nabla \cdot (\rho U h_{\text{tot}}) = \nabla \cdot (\lambda \nabla T) + S_E, \qquad h_{\text{tot}} = h + 0.5\left(U^2\right). \tag{8}$$

In these equations, ρ, t, U, P, δ, μ, S, H, λ, T are density, time, velocity, pressure, Kronecker delta function, viscosity, enthalpy, thermal conductivity, and fluid temperature, respectively. Also, S_M is the sum of internal forces entering the fluid domain.

In the solid environment, the main governing equation is the heat transfer equation. Assuming that the conduction is the primary heat transfer mechanism, the heat transfer equation in the solid media can be expressed as follows [43]:

$$\frac{\partial \rho C_P T}{\partial t} = \nabla \cdot (\lambda \nabla T) + S_E, \tag{9}$$

where C_P and S_E are thermal capacities and heat production term in the solid media, respectively. Also, the dynamic equations of motion in solid media for the spring-viscous-mass system are presented as the following equation [43]:

$$M\ddot{X} + C\dot{X} + KX = F(t), \tag{10}$$

where X, $\dot{X}$ and $\ddot{X}$ are displacement, first, and second derivatives of displacement relative to time, respectively. Also, M, C, K, F are mass, damper coefficient, spring coefficient, and external forces, respectively. For the two-way coupling, the coupling sub-solver relates the fluid and solid media through the following boundary conditions [43]:

$$U \cdot n = \dot{X} \cdot n, \tag{11}$$

$$U \times n = \dot{X} \times n, \tag{12}$$

$$\lambda_f (\nabla T \cdot n)_f = \lambda_S (\nabla T \cdot n)_S, \tag{13}$$

where n is the normal vector of the surface.

3.4. Description of damping model

Detonation waves can have strong impacts on solid bodies and create shock waves in the material. In order to handle the discontinuities associatedwith such shocks, viscous terms are introduced into the numerical method. These additional

terms spread out the shock discontinuities over several elements and thus allow the simulation to reach a smooth result. The used viscous terms in this study are based on the work of von Neumann, Richtmeyer, and Wilkins [44] and are presented in the form of Equation (14):

$$q = \begin{cases} \rho \left[\left(C_Q d \left(\dfrac{\dot{V}}{V} \right) \right)^2 - C_L c \left(\dfrac{\dot{V}}{V} \right) \right] & \text{for } \dfrac{\dot{V}}{V} \leqslant 0, \\ 0 & \text{for } \dfrac{\dot{V}}{V} > 0, \end{cases} \tag{14}$$

where C_Q and C_L are quadratic and linear artificial viscosity coefficient, respectively; d and $\dot{V}/V$ are average elements length and rate of change in volume; ρ and c are material density and local sound speed. In Equation (14), the quadratic term smoothes out shock discontinuities while the linear term acts to damp out oscillations.

Also, to avoid zero-energy modes of deformation, corrective forces (Hourglass forces) are added to the solution to resist the hourglass modes of deformation. The standard formulation for hourglass forces is based on the work of Kosloff and Frazier [45] and is defined as follows:

$$F_H = C_H \rho c V^{2/3} f_{KF} \left(\dot{X} \right), \tag{15}$$

where F_H and C_H are hourglass forces at each node of element and hourglass damping viscosity coefficient, respectively. Also, $f_{KF} \left(\dot{X} \right)$ is a vector of the element nodal velocities aligned with the hourglass shape factor. In Table 3, the values of these damping coefficients are presented.

Table 3.

Coefficients of damping model

Parameters	Value
Quadratic artificial viscosity coefficient	0.9
Linear artificial viscosity coefficient	0.2
Hourglass damping viscosity coefficient	0.1

3.5. Numerical model for material properties

Due to the sharp changes in pressure, and consequently, the volume of materials, it is necessary to have a relation to calculate the density of materials in explosion-related problems. In the present study, air behavior is determined using the ideal gas equation of state. This equation is the simplest and the most practical equation of state for predicting the behavior of gases which is expressed in terms of Boyle's and Gay-Lussac's law [42, 46]:

$$P\nu = RT, \tag{16}$$

where ν and R are specific volume and gas constant, respectively. To predict the water properties, the polynomial equation of state was used in the numerical model according to Equation (17) [47]:

$$P = \begin{cases} A_1\mu + A_2\mu^2 + A_3\mu^3 + (B_0 + B_1\mu)\, P_0 e & \text{in compression,} \\ T_1\mu + T_2\mu^2 + B_0 P_0 e & \text{in tension,} \end{cases} \tag{17}$$

where $\mu = \nu_0/\nu - 1$, P_0 is atmospheric pressure, and e is internal energy per unit mass, which can be described as follows:

$$e = (\rho g h + P_0) \,/\, (\rho B_0)\,, \tag{18}$$

in which ρ and h are density and depth of water, respectively. The values of empirical coefficients used for water are presented in Table 4 [47].

Table 4.

Coefficients of the polynomial equation of state for water [47]

Parameter	Value	Parameter	Value
Bulk modulus, A_1 (kPa)	2.20e6	Parameter T_2 (kPa)	0.00
Parameter A_2 (kPa)	9.54e6	Parameter B_1	0.28
Parameter A_3 (kPa)	1.45e7	Parameter B_0	0.28
Parameter T_1 (kPa)	2.20e6		

To predict explosive behavior, the JWL equation of state is used in the simulations. This empirical-mathematical expression has been introduced by Jones, Wilkins, and Lee [48] and is used to describe the relationship between the pressure, specific volume, and chemical energy of detonation products. It can be used to predict the properties of explosive charges up to the pressure of 100 MPa and can be described as follows [49, 50]:

$$P = A\left(1 - \frac{\omega\eta}{R_1}\right)\exp\left(-\frac{R_1}{\eta}\right) + B\left(1 - \frac{\omega\eta}{R_2}\right)\exp\left(-\frac{R_2}{\eta}\right) + \omega\rho e. \tag{19}$$

Here, $\eta = \nu_0/\nu$ and ν_0 is the initial specific volume of the explosive charge. The energy, e, includes chemical bond and kinetic energy. The terms A and B are the pressure coefficients; R_1 and R_2 are the principal and secondary eigenvalues, respectively. Also, ω is the fractional part of the normal Tait equation adiabatic exponent. To determine the value of these constants, the standard cylinder tests have been used. These empirical coefficients for the TNT explosive charge are presented in Table 5.

In materials such as steel, the gradient of specific volume due to pressure changes is insignificant. So, the linear equation of the state can predict the material properties with reasonable accuracy. In these materials, bulk modulus relates

Table 5.

Coefficients of JWL equation of state for the explosive charge (TNT) [48]

Parameter	Value	Parameter	Value
Parameter A (kPa)	3.71e8	Parameter R_2	0.95
Parameter B (kPa)	3.23e6	Parameter ω	0.00
Parameter R_1	4.15		

pressure and specific volume with the linear equation of state [51]:

$$K = -\nu \frac{\mathrm{d}P}{\mathrm{d}\nu}, \tag{20}$$

where K is the bulk modulus, which is considered equal to 1.58e9 kPa.

3.6. Failure and strength models

In materials that can withstand shear stress, the yield stress is used to determine the elastic or plastic state, which is a function of strain, strain rate, and temperature. In the Johnson-Cook strength equation, the yield stress is related to these parameters according to Equation (21) [49, 52]:

$$Y = \left[A + B\varepsilon_P^n\right]\left[1 + C\ln\varepsilon_P^*\right]\left[1 - T_H^m\right]. \tag{21}$$

In the above equation, the brackets describe the relation of yield stress to strain, strain rate, and temperature. The empirical coefficients of the Johnson-Cook strength equation for steel are shown in Table 6.

Table 6.

Coefficients of Johnson-Cook strength model for steel [53]

Parameter	Value	Parameter	Value
Yield stress, A (kPa)	4.99e5	Strain rate constant, C	7.90e−3
Hardening constant, B (kPa)	3.82e5	Thermal exponent, m	8.93e−1
Hardening exponent, n	0.46		

For damage prediction, the Johnson-Cook failure criterion was used in the constitutive model. This criterion is one of the most accurate and widespread models in failure theories that use failure parameter D. This parameter is defined as the ratio of failed area to total area. When it gets equal to unity, the ultimate fracture is anticipated. Johnson-Cook failure model defines D parameter as a function of plastic strain by following equation [54]:

$$D = \int \frac{1}{\varepsilon_f} \mathrm{d}\varepsilon_{eq}^P, \tag{22}$$

where ε_f is an equivalent strain to fracture and ε_{eq}^{p} is the equivalent plastic strain which can be calculated using the following equation [54]:

$$\varepsilon_f = \left[d_1 + d_2 e^{-d_3 \frac{\sigma_m}{\sigma_{vM}}}\right]\left[1 + d_4 \ln\left(\frac{\dot{\varepsilon}_{eq}^{P}}{\dot{\varepsilon}_0}\right)\right], \tag{23}$$

where σ_m, σ_{vM} and $\dot{\varepsilon}_0$ are the average of the three normal stresses, the Von-Mises equivalent stress, and a reference strain rate, respectively. Equations (22) and (23) indicate that the Johnson-Cook failure model depends on the strain, strain rate, and temperature. The empirical constants of this model for steel are shown in Table 7. So, in the numerical model the failure parameter in each element is calculated and when it reaches to unity, the erosion will be expected.

Table 7.

Material constants of Johnson-Cook failure model for steel [53]

Parameter	Value	Parameter	Value
Parameter, d_1	0.35	Parameter, d_4	−0.02
Parameter, d_2	0.28	Parameter, d_5	0.02
Parameter, d_3	−0.11		

4. Results and discussion

4.1. Grid independence analysis

In this study, to ensure that the results were independent of grid sizes, four different grid structures were generated, according to Table 8. This table presents the number and the length of elements for each of the four grid types. Results of the grid independency analysis are presented in Fig. 8. In this figure, the pressure diagram was plotted versus time at gauge points #1 and #2. The results indicate that refinement of the grid number 3 with 20,000 elements has a negligible influence on the numerical results. Therefore, to reduce the numerical costs, all simulations were performed using grid number 3.

Table 8.

Details of grid independence analysis

Grid number	Number of elements	Element length (mm)
#1	5000	2.00
#2	10000	1.00
#3	20000	0.50
#4	30000	0.33

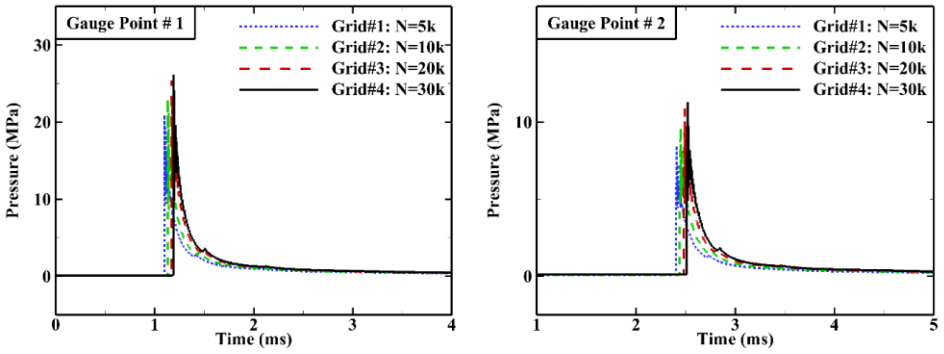

Fig. 8. Pressure-time curves at gauge points #1 and #2 – numerical results for different grid sizes

4.2. Unconfined UNDEX

To qualitatively and quantitatively investigate the structure of blast waves in UNDEX as well as verification of the numerical method, the results of numerical simulations and empirical formula [1] were compared in Fig. 9. In this figure, the pressure-time curves are presented at gauge points 1 to 4 (with distances of 2, 4, 6, and 8 m from the detonation point). In these graphs, the empirical results

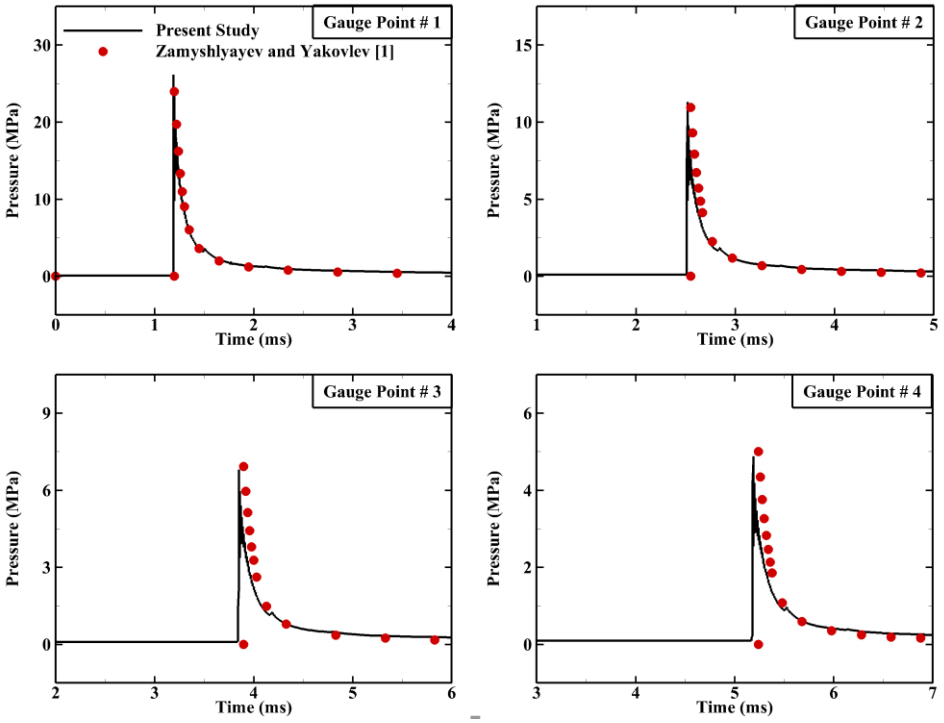

Fig. 9. Pressure-time curves at the gauge points – numerical results along with empirical results

[1] and the numerical results were distinguished by red dots and black lines, respectively. The results reveal that just 1.2 ms after the explosion, the blast wave reaches the first gauge point, and the pressure of this region was abruptly increased to its maximum value of 24 MPa. Afterward, the pressure decreased gradually and got balanced with the ambient condition. The blast wave was created due to the instantaneous energy release of the explosive charge, which increased the temperature and pressure of the surrounding area. Intensified pressure in the near-explosion area led to the formation of the shock wave in the environment with a velocity of 1650 m/s. Hence, the blast wave moves with supersonic velocity, and the targets in the downstream do not receive any warning before imminent destruction. The same trend was repeated in the gauge points #2, #3, and #4. In these points, the maximum pressure amplitudes are reduced to 11, 7, and 5 MPa, respectively. Moreover, the pressure-time curves calculated by empirical formula [1] are in good agreement with those obtained by numerical simulations confirming the validity of the numerical method.

For a detailed analysis of UNDEX, pressure-time curves were plotted at different gauge points, i.e., points #1 to #4, as shown in Fig. 10. Accordingly, it is clear that the compressive pressure wave reached the desired points abruptly and without any notice. In other words, while the fluid pressure is zero, a sharp jump in pressure was created instantly after the arrival of the blast wave. Then, the pressure was gradually reduced and became in equilibrium with ambient. In other words, in the UNDEX, the blast wave is characterized by a sudden pressure jump at the shock front, followed by a quasi-exponential decrement back to the ambient value. The results also showed that the pressure amplitude is in inverse proportion with distance from the explosion point.

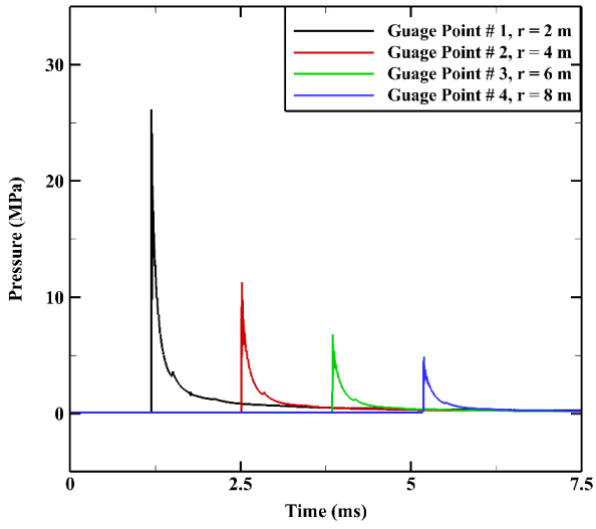

Fig. 10. Pressure-time curves at 2, 4, 6 and 8 m distance from explosion point

For qualitative analysis, pressure contours at different times after the explosion occurred are presented in Fig. 11. According to the results, it can be observed that instantly after the explosion, the compressive pressure waves were created in the water environment. The shock wave sweeps half of the numerical domain with the supersonic speed in less than 4 ms. Hence, it kicks any targets in the environment without any prior warning. The results show that with the expansion of the blast wave in the environment, the pressure amplitude decreased gradually and reached to 9 MPa at $t = 2$ ms. Also, scrutiny of the results indicates that the boundary conditions have been set properly. In other words, there is no pressure reflection in the boundaries, which was expected in an unconfined UNDEX.

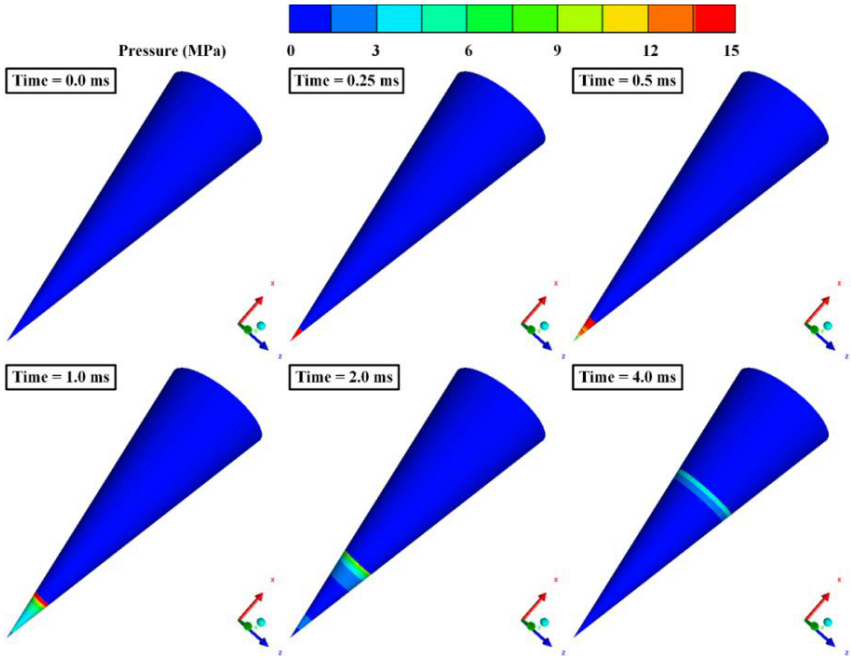

Fig. 11. Pressure contours at different times after the explosion

4.3. UNDEX effects on a reinforced plate

After analyzing the structure and growth of an explosive wave in water environments, its effect on a steel structure reinforced with perpendicular blades was investigated. For this purpose, in Fig. 12, Von-Mises stress contours are shown at various times after the explosion. The results show that the center of the reinforced steel plate was the first area having an abrupt increase in Von-Mises stress. Then, the stress was propagated to a wider area on the plate. By the spatial growth of the explosion, the plate was pushed and moved downward. Hence, due to the fixed boundaries, the stress has increased in the borders. By exceeding the plate yield stress, the plate was failed and torn off at the corners ($t = 0.96$ ms). Results indicate

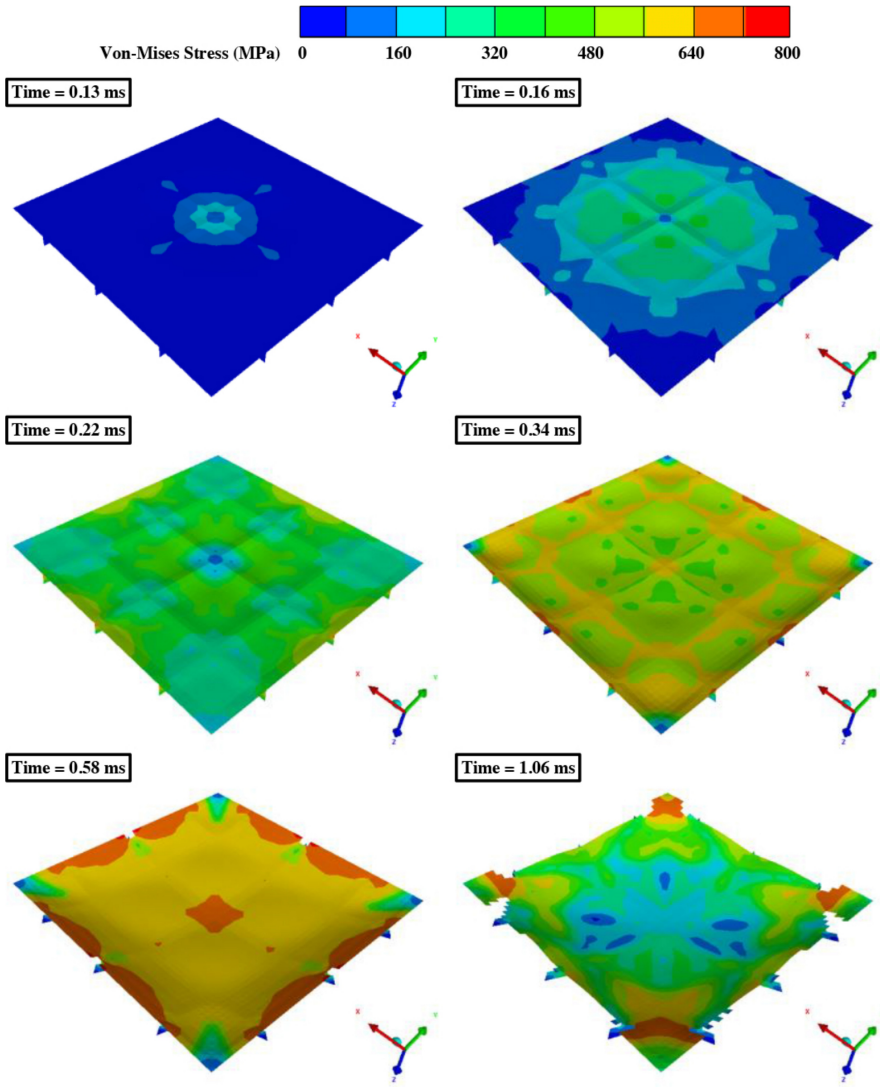

Fig. 12. Von-Mises stress contours of the reinforced plate at different times after the explosion

that the stiffeners can reasonably increase the strength of the plate and prevent the failure of the central parts of the plate.

In Fig. 13, strain contours are shown at different times after the explosion. In this figure, it is evident that, first of all, the middle part of the plate was deformed. With the growth of the pressure wave, the edges of the plate were also affected. The results show that, after $t = 0.48$ ms, the amount of strain on the area near the fixed borders exceeded the tolerable limit and torn the corners parts.

To further analyze the results, the displacement-time and displacement rate-time curves at the center of the reinforced plate are shown in Fig. 14. In this figure,

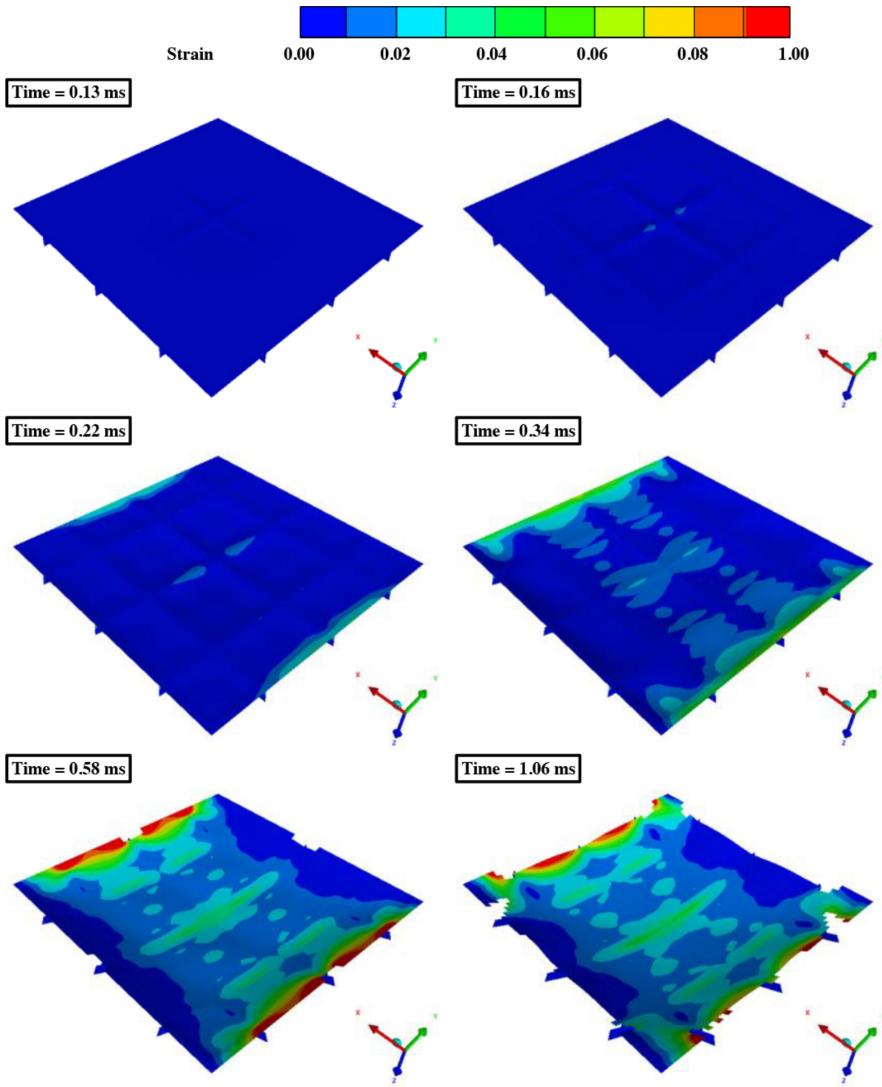

Fig. 13. Strain contours of the reinforced plate at different times after the explosion

the displacement and displacement rate curves were plotted with a continuous black line and red dashed line, respectively. The results show that the UNDEX deformed the plate and moved the center part about 90 mm in just 1.8 ms. Also, the results revealed that the displacement rate increases sharply at initial moments and reached its maximum value of 135 mm/ms at $t = 0.34$ ms. Afterward, due to the decay of the energy of explosive charge, the displacement rate decreased gradually and oscillated around 25 mm/ms.

For a better analysis of the results, this section examines the propagation of the blast wave in the water environment. Fig. 15 and Fig. 16 show the blast wave

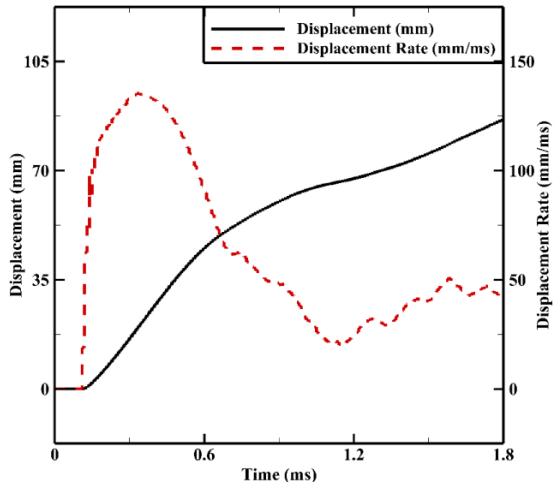

Fig. 14. Displacement & displacement rate-time curves at the center point of the reinforced plate

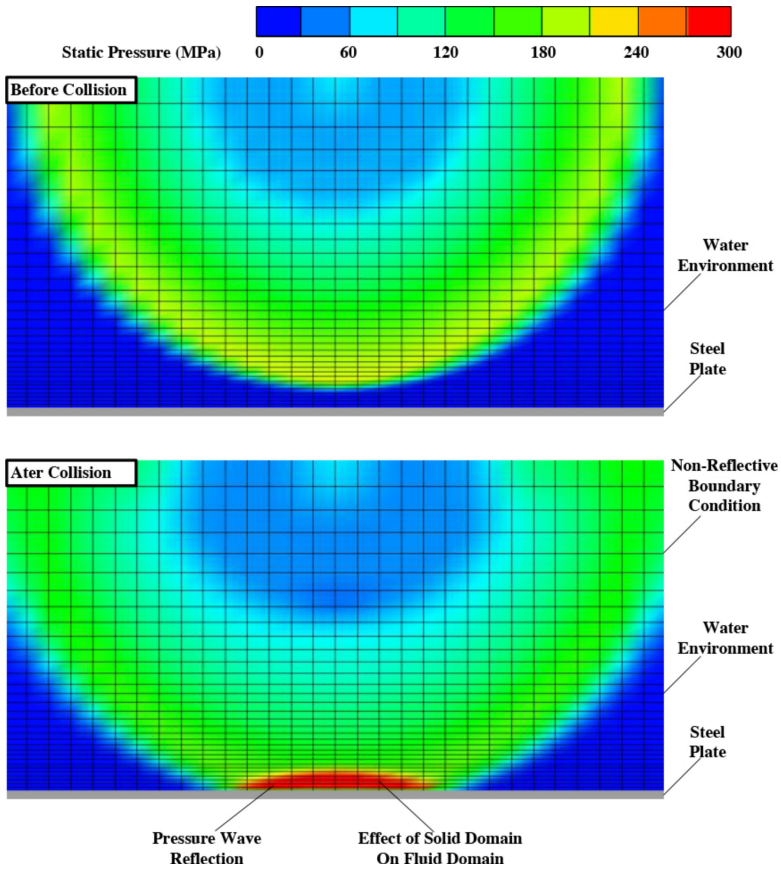

Fig. 15. Blast wave propagation and interaction with structure at plane $x = 0$

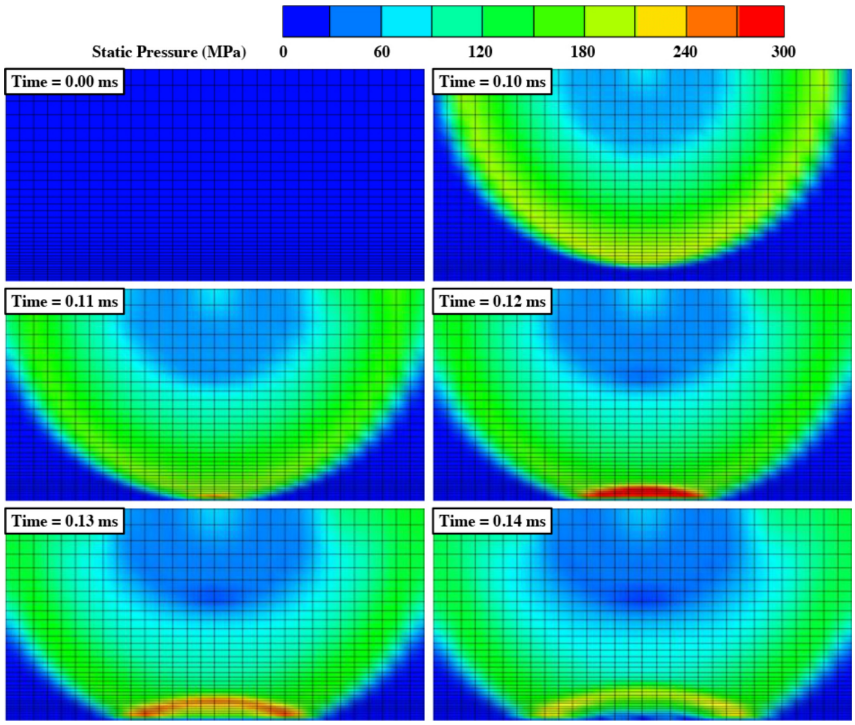

Fig. 16. Static pressure contours at plane $x = 0$ at different moments

propagation and interaction with structure in the Eulerian environment at plane $x = 0$. The results show that in the initial moments, the blast wave was propagated spherically in all directions (before the collision). Next, with the impact of the blast wave with the steel plate, the symmetry of the pressure wave disappeared. In this moment, part of incident wave was reflected and the rest of it was transmitted through the plate. It can also be found that the pressure waves from side boundaries were transmitted without any reflection (unlimited water domain). However, at the lower boundary where the water is in contact with the steel plate, the pressure wave was reflected inside the numerical domain. It should be noted that the reflected pressure wave is 3.5–4 time higher than incident pressure wave which is in accordance with previous studies [23, 55, 56]. These results indicate that boundary conditions were in accordance with the physics of the problem and were well defined in the numerical model.

5. Conclusions

In this paper, the generated shock wave due to the explosion of TNT in the water environment was simulated, and its effect on steel structures reinforced with perpendicular blades was also investigated using numerical methods. It was found

that in an unconfined UNDEX, a supersonic pressure wave (with velocity about 1650 m/s) sweeps the water environment, resulting in an abrupt increase in static pressure up to 24 MPa. Therefore, the targets in the downstream do not receive any warning before the collision. Also, the evaluation of the empirical solution for UNDEX and numerical results indicated that the employed numerical method predicted the structure of the blast wave with satisfactory accuracy. Moreover, the results of FSI simulations specified that due to the collision of the explosive wave with the steel structure, it reflected and increased the stress at the plate. The reflected pressure wave was propagated through water, supporting initial waves. The results revealed that using perpendicular blades as a stiffener is an acceptable method for improvement of the strength. Also, the results showed that with the explosion of 500 g of TNT at a distance of 260 m, maximum displacement and displacement rate of the plate reached to 90 mm (at $t = 2.8$ ms) and 135 mm/ms (at $t = 1.24$ ms), respectively. For further analysis, it is recommended to perform a parametric study to determine the effect of stiffeners' breadth, length, and arrangements on the ultimate resistance. This study will help to design a high resistance structure against UNDEX.

Manuscript received by Editorial Board, September 09, 2019;
final version, February 10, 2020.

References

[1] B.V. Zamyshlyaev and Y.S. Yakovlev. *Dynamic loads in underwater explosion*, Naval Intelligence Support Center Washington, D.C, 1973.

[2] N.A. Fleck and V.S. Deshpande. The resistance of clamped sandwich beams to shock loading. *Journal of Applied Mechanics*, 71(3):386–401, 2004. doi: 10.1115/1.1629109.

[3] X. Qiu, V.S. Deshpande, and N.A. Fleck. Dynamic response of a clamped circular sandwich plate subject to shock loading. *Journal of Applied Mechanics*, 71(5):637–645, 2004. doi: 10.1115/1.1778416.

[4] L. Ren, H. Ma, Z. Shen, and Y. Wang. Blast response of water-backed metallic sandwich panels subject to underwater explosion – Experimental and numerical investigations. *Composite Structures*, 209:79–92, 2019. doi: 10.1016/j.compstruct.2018.10.082.

[5] W. Johnson, A. Poynton, H. Singh, and F.W. Travis. Experiments in the underwater explosive stretch forming of clamped circular blanks. *International Journal of Mechanical Sciences*, 8(4):237–270, 1966. doi: 10.1016/0020-7403(66)90027-0.

[6] W. Cao, Z. He, and W. Chen. Experimental study and numerical simulation of the afterburning of TNT by underwater explosion method. *Shock Waves*, 24(6):619–624, 2014. doi: 10.1007/s00193-014-0527-2.

[7] K. Liu, Z. Wang, W. Tang, Y. Zhang, and G. Wang. Experimental and numerical analysis of laterally impacted stiffened plates considering the effect of strain rate. *Ocean Engineering*, 99:44–54, 2015. doi: 10.1016/j.oceaneng.2015.03.007.

[8] J.M. Gordo, C. Guedes Soares, and D. Faulkner. Approximate assessment of the ultimate longitudinal strength of the hull girder. *Journal of Ship Research*, 40(1):60–69, 1996.

[9] Z. Zhang, L. Wang, and V.V. Silberschmidt. Damage response of steel plate to underwater explosion: Effect of shaped charge liner. *International Journal of Impact Engineering*, 103:38–49, 2017. doi: 10.1016/j.ijimpeng.2017.01.008.

[10] Z. Jin, C. Yin, Y. Chen, and H. Hua. Numerical study on the interaction between underwater explosion bubble and a moveable plate with basic characteristics of a sandwich structure. *Ocean Engineering*, 164:508–520, 2018. doi: 10.1016/j.oceaneng.2018.07.001.

[11] C. Xin, G. Xu., and K. Liu. Numerical simulation of underwater explosion loads. *Transactions of Tianjin University*, 14(suppl.1):519–522, 2008. doi: 10.1007/s12209-008-0089-4.

[12] E. Gauch, J. LeBlanc, and A. Shukla. Near field underwater explosion response of polyurea coated composite cylinders. *Composite Structures*, 202:836–852, 2018. doi: 10.1016/j.compstruct.2018.04.048.

[13] F. Vannucchi de Camargo. Survey on experimental and numerical approaches to model underwater explosions. *Journal of Marine Science and Engineering*, 7(1):1–18, 2019. doi: 10.3390/jmse7010015.

[14] B.G. Prusty and S.K. Satsangi. Analysis of stiffened shell for ships and ocean structures by finite element method. *Ocean Engineering*, 28(6):621–638, 2001. doi: 10.1016/S0029-8018(00)00021-4.

[15] N.K. Gupta, P. Kumar, and S. Hegde. On deformation and tearing of stiffened and un-stiffened square plates subjected to underwater explosion – a numerical study. *International Journal of Mechanical Sciences*, 52(5):733–744, 2010. doi: 10.1016/j.ijmecsci.2010.01.005.

[16] Z.H. Ma, D.M. Causon, L. Qian, H.B. Gu, C.G. Mingham, and P. Martinez Ferrer. A GPU based compressible multiphase hydrocode for modelling violent hydrodynamic impact problems. *Computers & Fluids*, 120:1–23, 2015. doi: 10.1016/j.compfluid.2015.07.010

[17] G. Wang, Y. Wang, W. Lu, W. Zhou, M. Chen, and P. Yan. On the determination of the mesh size for numerical simulations of shock wave propagation in near field underwater explosion. *Applied Ocean Research*, 59:1–9, 2016. doi: 10.1016/j.apor.2016.05.011.

[18] S. Li, R. Han, A.M. Zhang, and Q.X. Wang. Analysis of pressure field generated by a collapsing bubble. *Ocean Engineering*, 117:22–38, 2016. doi: 10.1016/j.oceaneng.2016.03.016.

[19] G. Beer. Finite element, boundary element and coupled analysis of unbounded problems in elastostatics. *International Journal for Numerical Methods in Engineering*, 19(4):567–580, 1983. doi: 10.1002/nme.1620190408.

[20] S.W. Gong and B.C. Khoo. Transient response of stiffened composite submersible hull to underwater explosion bubble. *Composite Structures*, 122:229–238, 2015. doi: 10.1016/j.compstruct.2014.10.026.

[21] T. De Vuyst, K. Kong, N. Djordjevic, R. Vignjevic, J.C. Campbell, and K. Hughes. Numerical modelling of the effect of using multi-explosives on the explosive forming of steel cones. *Journal of Physics: Conference Series*, 734:032074, 2016. doi: 10.1088/1742-6596/734/3/032074.

[22] F.R. Ming, A.M. Zhang, Y.Z. Xue, and S.P. Wang. Damage characteristics of ship structures subjected to shockwaves of underwater contact explosions. *Ocean Engineering*, 117:359–382, 2016. doi: 10.1016/j.oceaneng.2016.03.040.

[23] O. Adibi, A. Azadi, B. Farhanieh, and H. Afshin. A parametric study on the effects of surface explosions on buried high pressure gas pipelines. *Engineering Solid Mechanics*, 5(4):225–244, 2017. doi: 10.5267/j.esm.2017.9.003.

[24] C. Hesch and P. Betsch. Continuum mechanical considerations for rigid bodies and fluid-structure interaction problems. *Archive of Mechanical Engineering*, 60(1):95–108, 2013. doi: 10.2478/meceng-2013-0006.

[25] G. Wang and S. Zhang. Damage prediction of concrete gravity dams subjected to underwater explosion shock loading. *Engineering Failure Analysis*, 39:72–91, 2014. doi: 10.1016/j.engfailanal.2014.01.018.

[26] H. Linsbauer. Hazard potential of zones of weakness in gravity dams under impact loading conditions. *Frontiers of Architecture and Civil Engineering in China*, 5(1):90–97, 2011. doi: 10.1007/s11709-010-0008-3.

[27] S. Zhang, G. Wang, C. Wang, B. Pang, and C. Du. Numerical simulation of failure modes of concrete gravity dams subjected to underwater explosion. *Engineering Failure Analysis*, 36:49–64, 2014. doi: 10.1016/j.engfailanal.2013.10.001.

[28] R. Rajendran. Numerical simulation of response of plane plates subjected to uniform primary shock loading of non-contact underwater explosion. *Materials & Design*, 30(4):1000–1007, 2009. doi: 10.1016/j.matdes.2008.06.054

[29] A.M. Zhang, L.Y. Zeng, X.D. Cheng, S.P. Wang, and Y. Chen. The evaluation method of total damage to ship in underwater explosion. *Applied Ocean Research*, 33(4):240–251, 2011. doi: 10.1016/j.apor.2011.06.002.

[30] E. Fathallah, H. Qi, L.Tong, and M. Helal. Numerical simulation and response of stiffened plates subjected to noncontact underwater explosion. *Advances in Materials Science and Engineering*, 2014:752586, 2014. doi: 10.1155/2014/752586.

[31] J. Qiankun and D. Gangyi. A finite element analysis of ship sections subjected to underwater explosion. *International Journal of Impact Engineering*, 38(7):558–566, 2011. doi: 10.1016/j.ijimpeng.2010.11.005.

[32] G. Wang, S. Zhang, M. Yu, H. Li, and Y. Kong. Investigation of the shock wave propagation characteristics and cavitation effects of underwater explosion near boundaries. *Applied Ocean Research*, 46:40–53, 2014. doi: 10.1016/j.apor.2014.02.003.

[33] J. LeBlanc and A. Shukla. The effects of polyurea coatings on the underwater explosive response of composite plates. In S. Gopalakrishnan and Y. Rajapakse, editors, *Blast Mitigation Strategies in Marine Composite and Sandwich Structures*, pages 53–72, Springer, 2018. doi: 10.1007/978-981-10-7170-6_3.

[34] H. Huang, Q.J. Jiao, J.X. Nie, and J.F. Qin. Numerical modeling of underwater explosion by one-dimensional ANSYS-AUTODYN. *Journal of Energetic Materials*, 29(4):292–325, 2011. doi: 10.1080/07370652.2010.527898.

[35] A. Schiffer. The response of submerged structures to underwater blast. Ph.D. Thesis, Oxford University, UK, 2013.

[36] R.D. Ambrosini and B.M. Luccioni. Craters produced by explosions on the soil surface. *Journal of Applied Mechanics*, 73(6):890–900, 2006. doi: 10.1115/1.2173283.

[37] G. Hou, J. Wang, and A. Layton. Numerical methods for fluid-structure interaction – a review. *Communications in Computational Physics*, 12(2):337–377, 2012. doi: 10.4208/cicp.291210.290411s.

[38] H.-J. Bungartz, M. Mehl, and M. Schäfer. *Fluid Structure Interaction II: Modelling, Simulation, Optimization*. Springer-Verlag Berlin Heidelberg, 2010.

[39] A. Pazouki, R. Serban, and D. Negrut. A high performance computing approach to the simulation of fluid-solid interaction problems with rigid and flexible components. *Archive of Mechanical Engineering*, 61(2):227–251, 2014. doi: 10.2478/meceng-2014-0014.

[40] N.K. Birnbaum, J.N. Francis, and B.I. Gerber. Coupled techniques for the simulation of fluid-structure and impact problems. *Computer Assisted Mechanics and Engineering Sciences*, 6(3/4):295–311, 1999.

[41] P. Sherkar, A.S. Whittaker, and A.J. Aref. Modeling the effects of detonations of high explosives to inform blast-resistant design. Technical Report MCEER-10-0009, 2010.

[42] Y.A. Çengel and M.A. Boles. *Thermodynamics: An Engineering Approach*. McGraw-Hill, 2002.

[43] J.C. Jo. Fluid-structure interactions. In Y.W. Kwon and P-S. Lam, editors, *Pressure Vessels and Piping Systems*. Encyclopedia of Life Support Systems (EOLSS), 2004.

[44] M.L. Wilkins. Use of artificial viscosity in multidimensional fluid dynamic calculations. *Journal of Computational Physics*, 36(3):281–303, 1980. doi: 10.1016/0021-9991(80)90161-8.

[45] D. Kosloff and G.A. Frazier. Treatment of hourglass patterns in low order finite element codes. *International Journal for Numerical and Analytical Methods in Geomechanics*, 2(1):57–72, 1978. doi: 10.1002/nag.1610020105.

[46] O. Adibi, B. Farhanieh, and H. Afshin. Numerical study of heat and mass transfer in under-expanded sonic free jet. *International Journal of Heat and Technology*, 35(4):959–968, 2017. doi: 10.18280/ijht.350432.

[47] L.H. Bakken and P.D. Anderson. The complete equation of state handbook. Technical Report SCL-TM-67-118, Sandia Corporation, Livermore, USA, 1967.

[48] G. Baudin and R. Serradeill. Review of Jones-Wilkins-Lee equation of state. *EPJ Web of Conferences*, 10:00021, 2010. doi: 10.1051/epjconf/20101000021.

[49] A. Dacko and J. Toczyski. Vulnerability analysis of aircraft fuselage subjected to internal explosion. *Archive of Mechanical Engineering*, 58(4):393–406, 2011. doi: 10.2478/v10180-011-0024-4.

[50] A. Morka, P. Kedzierski, and R. Gieleta. Selected aspects of numerical analysis of layered flexible structures subjected to impact of soft core projectile. *Archive of Mechanical Engineering*, 62(1):73–83, 2015. doi: 10.1515/meceng-2015-0005.

[51] D.J. Steinberg, S.G. Cochran, and M.W. Guinan. A constitutive model for metals applicable at high-strain rate. *Journal of Applied Physics*, 51(3):1498–1504, 1980. doi: 10.1063/1.327799.

[52] G.R. Johnson and W.H. Cook. A constitutive model and data for materials subjected to large strains, high strain rates, and high temperatures. Proceedings of 7th International Symposium on Ballistics, pages 541–547, Hague, The Netherlands, 1983.

[53] G.R. Johnson and W.H. Cook. Fracture characteristics of three metals subjected to various strains, strain rates, temperatures and pressures. *Engineering Fracture Mechanics*, 21(1):31–48, 1985. doi: 10.1016/0013-7944(85)90052-9.

[54] O. Björklund. Modelling of failure. M.Sc. Thesis, Linköping University, Linköping, Sweden, 2008.

[55] L. Mazurkiewicz, J. Malachowski, and P. Baranowski. Blast loading influence on load carrying capacity of I-column. *Engineering Structures*, 104:107–115, 2015. doi: 10.1016/j.engstruct.2015.09.025.

[56] P. Baranowski, J. Malachowski, and L. Mazurkiewicz. Numerical and experimental testing of vehicle tyre under impulse loading conditions. *International Journal of Mechanical Sciences*, 106:346–356, 2016. doi: 10.1016/j.ijmecsci.2015.12.028.